ACS Energy LETTERS

http://pubs.acs.org/journal/aelccp

Letter

Tuning Self-Assembled Monolayers of Me-4PACz with Bisphosphonic Acid Groups to Improve Temperature and Cycling Stability of Perovskite Photovoltaics

Haonan Sun,[&] Guibin Shen,[&] Huei Min Chua, Darrell Jun Jie Tay, Yuanjie Su, Yahong Pu, Yanju Wang, Yeow Boon Tay, Hongkang Fu, Subodh G. Mhaisalkar, Shixuan Du, Nripan Mathews,* and Wei Lin Leong*

Cite This: *ACS Energy Lett.* 2026, 11, 3755−3763

Read Online

ACCESS | Metrics & More | Article Recommendations | Supporting Information

ABSTRACT: Buried interface quality in p-i-n perovskite solar cells (PSCs) is shown to improve via the use of a mixed self-assembled monolayer (SAM) of [4-(3,6-dimethyl-9*H*-carbazol-9-yl)butyl]phosphonic acid (Me-4PACz) and (9H,9′H-[3,3′-bicarbazole]-9,9′-diylbis(butane-4,1-diyl))diphosphonic acid (Bi4PACz), eschewing the need for a NiO_x layer. The bisphosphonic acid-based Bi4PACz minimizes SAM aggregation and enhances the wettability and uniformity. It also coordinates with the perovskite, passivating defects and suppressing PbI_2 aggregation, thereby minimizing recombination losses. The improved buried interface quality leads to power conversion efficiencies (PCEs) of 24.48%, 25.65%, and 22.60% for triple cation PSCs with bandgaps of 1.61, 1.58, and 1.68 eV, respectively, demonstrating the wide applicability of this approach. Under temperature conditions, the PSCs retained 84% of initial PCE after 1200 h at 85 °C and 97% after 250 thermal cycles (−40 to +70 °C), indicating its potential for space-related applications. This mixed-SAM approach establishes a universal pathway toward efficient and temperature-stable perovskite photovoltaics.

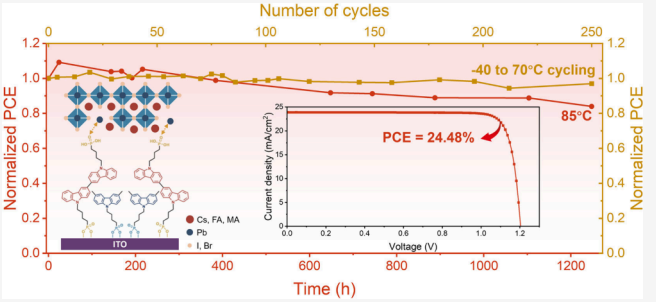

Perovskite solar cells (PSCs) of a p-i-n architecture are of great interest due to their high efficiency, excellent stability, low cost, low-temperature processing, and compatibility with tandem architectures[1] with power conversion efficiencies (PCEs) of 27% noted.[2,3] Current p-i-n PSCs typically adopt self-assembled monolayers (SAMs) as hole transport layers (HTLs), such as [2-(9*H*-carbazol-9-yl)ethyl]-phosphonic acid (2PACz), [2-(3,6-dimethoxy-9*H*-carbazol-9-yl)ethyl]phosphonic acid (MeO-2PACz), and [4-(3,6-dimethyl-9*H*-carbazol-9-yl)butyl]phosphonic acid (Me-4PACz).[1,4] Among them, Me-4PACz theoretically offers the fastest hole transfer rate and a low interface trap density at the buried interface, suggesting a reduction in nonradiative recombination.[5] However, its inhomogeneous distribution on substrates like indium tin oxide (ITO)[6,7] as well as hydrophobicity[8−10] often leads to pinholes, which result in severe energy losses at buried interfaces.[11] Furthermore, perovskite films grown on Me-4PACz may also tend to accumulate PbI_2 at the buried interface, deteriorating the interface contact and accelerating the perovskite degradation.[12,13]

Several strategies have been developed to improve the wettability of Me-4PACz, such as mixing with other molecules,[8,9,14,15] blending with conjugated polyelectrolytes,[8] and inserting an interfacial Al_2O_3 nanoparticulate layer as pinning sites to improve perovskite coverage.[14] NiO_x has been shown to be a suitable surface to promote a homogeneous distribution of Me-4PACz molecules, thereby enabling a denser and more uniform layer.[15,16] The potential of mixing Me-4PACz with the bisphosphonic acid SAM to strengthen perovskite/NiO_x interfaces has also been explored,[17] which provided valuable insights into interfacial bonding and device stability. Nonetheless, the involvement of metal-oxide interlayers such as NiO_x introduces additional variables. Variations in NiO_x synthesis can influence its energy levels,[18] which makes it challenging to discern the solar cell performance enhancement attributable solely to the interfacial SAM/NiO_x effects.[18−20] The interaction between Ni^{3+} and the organic cations of perovskite[21,22] may also induce interfacial recombination and accelerate degradation.[23]

In this work, we studied a co-self-assembly strategy, where Me-4PACz was mixed with (9*H*,9′*H*-[3,3′-bicarbazole]-9,9′-diylbis(butane-4,1-diyl))diphosphonic acid (Bi4PACz), a

Received: November 3, 2025
Revised: March 9, 2026
Accepted: April 7, 2026
Published: April 10, 2026

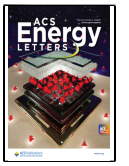

double-end SAM with an additional phosphonic acid group. By focusing on a direct, NiO_x-free ITO/SAM/perovskite buried interface, this approach allows the intrinsic effects of co-SAM chemistry on molecular assembly, buried-interface quality, and degradation behavior to be examined. The incorporation of Bi4PACz is demonstrated to minimize SAM aggregation, facilitating more homogeneous SAM deposition directly on ITO substrates. The improved SAM wettability enables a complete and uniform perovskite coverage without extra intermediate layers. The Me:Bi4PACz layer enhances the perovskite buried interface quality, with suppressed trap density, PbI_2 aggregation, and recombination losses. Importantly, this work further correlates co-SAM-regulated buried-interface chemistry with postaging structural evolution, clarifying how the co-SAM modifies the dominant thermal degradation pathway. Consequently, p-i-n PSC with a $Cs_{0.05}(FA_{0.85}MA_{0.15})_{0.95}Pb(I_{0.85}Br_{0.15})_3$ absorption layer (1.61 eV bandgap) achieved an outstanding PCE of 24.48%. In addition, the PSCs exhibited remarkably enhanced long-term stability, retaining over 84% of the initial PCE after 1200 h of continuous heating at 85 °C. Furthermore, the device retained 97% of the initial PCE after 250 thermal cycles between −40 and +70 °C, demonstrating its potential for space-related applications. This study therefore establishes a co-SAM framework that links molecular assembly, buried-interface degradation pathways, and device robustness directly on ITO substrates, offering a promising route toward high-performance, stable, and reproducible PSCs.

In contrast to conventional SAMs such as Me-4PACz (Figure 1a), Bi4PACz (Figure 1b) possesses an additional phosphonic acid group. In Me-4PACz, the phosphonic acid group anchors to ITO,[24] while the functional headgroup (carbazole) and alkyl chain linking group are exposed. For Bi4PACz, anchoring leaves the additional phosphate acid group extending outward,[25] allowing it to interact with the perovskite phase (Figure 1c). This hydrophilic phosphate acid group could enhance wettability, which would lead to better uniformity while also coordinating with perovskite to passivate defects. To form the SAM blend (Me:Bi4PACz), the Me-4PACz and Bi4PACz ethanol solutions (0.5 mg/mL each) are mixed (typically Me-4PACz:Bi4PACz = 5:1 v/v) before spin-coating onto the ITO.

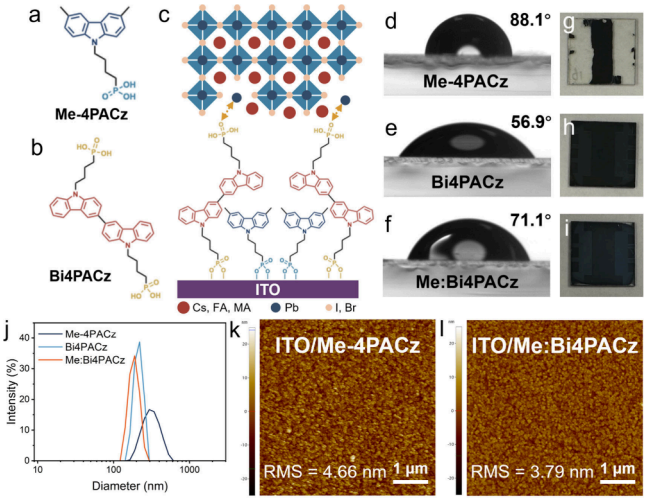

Figure 1. (a, b) Molecular structure of Me-4PACz and Bi4PACz. (c) Schematic illustration of the Me:Bi4PACz co-SAM between ITO and perovskite. (d–f) Contact angles of Me-4PACz, Bi4PACz, and Me:Bi4PACz on ITO substrates. (g–i) Photographs of perovskite spin-coated on Me-4PACz, Bi4PACz, and Me:Bi4PACz SAMs. (j) DLS micellar size distributions of Me-4PACz, Bi4PACz, and Me:Bi4PACz in ethanol with a concentration of 0.5 mg/mL. The hydrodynamic diameters are around 300, 220, and 190 nm for Me-4PACz, Bi4PACz, and Me:Bi4PACz solutions, respectively. (k, l) AFM height images of (k) ITO/Me-4PACz and (l) ITO/Me:Bi4PACz.

The anchoring of Me-4PACz greatly enhances the ITO hydrophobicity,[8,11,14,26] as evidenced by a large contact angle of 88.1° (Figure 1d) versus 10.1° for bare ITO (Figure S1). In contrast, Bi4PACz has a significantly smaller contact angle of 56.9° due to its exposed hydrophilic phosphate acid group (Figure 1e),[27] while Me:Bi4PACz exhibits an intermediate value of 71.1° (Figure 1f). The perovskite coverage correlates with the hydrophilicity: nonuniform perovskite coverage is observed on ITO/Me-4PACz (Figure 1g), whereas Bi4PACz and Me:Bi4PACz layers yield uniform coverage (Figure 1h and i).[11] This poor coverage on Me-4PACz can create performance and reproducibility challenges due to shunting effects.[16]

Due to the amphiphilic nature of SAMs, aggregation and micelle formation often occur in solutions, requiring extra effort to break micelles for SAM deposition during spin-coating, which may result in nonuniform SAM coverage[28] and interfacial losses.[29] To study the effect of Bi4PACz on reducing the aggregation of SAMs in ethanol solution, dynamic light scattering (DLS) was applied to evaluate the hydrodynamic diameters of the SAMs and their mixtures (Figure 1j). The hydrodynamic diameters of aggregates formed by Me-4PACz (~300 nm) and Bi4PACz (~220 nm) in ethanol decreased to ~190 nm upon mixing, indicating that Bi4PACz effectively reduces the molecular aggregation in the solution.[29] This reduced aggregation tendency can be attributed to the molecular characteristics of Bi4PACz, including its biphosphonic acid groups and extended conjugation, which favor stronger intermolecular interactions and discourage the formation of large aggregates. In particular, dual-head amphiphiles usually have higher critical aggregation concentrations than their single-head counterparts.[30,31] The $\pi-\pi$ stacking between the carbazole groups further stabilizes dispersed molecules,[32] alleviating micelle formation and enabling more uniform SAM coverage during spin-coating. To further elucidate the molecular mechanism by which Bi4PACz suppresses the aggregation of Me-4PACz, the intermolecular interaction patterns in Me-4PACz homodimers and Bi4PACz/Me-4PACz heterodimers were systematically investigated through DFT binding-energy calculations (Supplementary Note 1). The optimized geometries and corresponding binding energies are summarized in Figure S2. The Bi4PACz/Me-4PACz heterodimer configurations exhibit systematically lower binding energies than the Me-4PACz homodimer counterparts, while hetero-1 (synergistic double hydrogen bonding and carbazole ring conjugation) is the most stable structure with the lowest energy. These results confirm that the extended planar conjugation in Bi4PACz enhances the $\pi-\pi$ stacking efficiency. The synergistic combination of double hydrogen bonding and carbazole $\pi-\pi$ stacking between Bi4PACz and Me-4PACz effectively suppresses the aggregation behavior of Me-4PACz.

The existence of both SAMs on ITO can be evidenced by attenuated total reflection Fourier transform infrared spectroscopy (ATR-FTIR) results (Figure S3). Atomic force

https://doi.org/10.1021/acsenergylett.5c03637
ACS Energy Lett. 2026, 11, 3755−3763

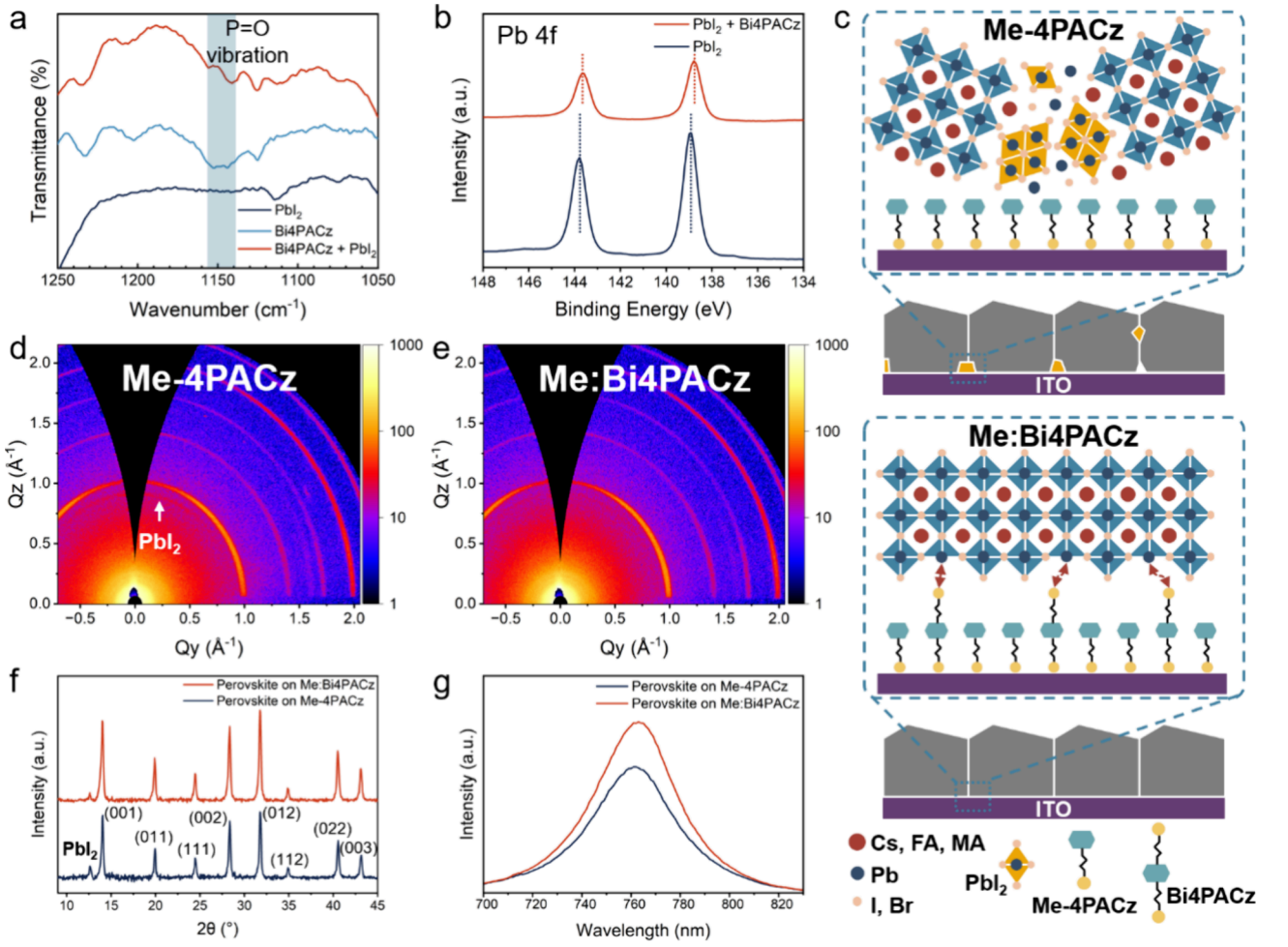

Figure 2. (a) ATR-FTIR spectra of PbI_2, Bi4PACz, and Bi4PACz + PbI_2 on ITO. (b) XPS spectra of Pb 4f in PbI_2 films without and with Bi4PACz. (c) Schematic of perovskite film quality improvement by Me:Bi4PACz. (d, e) Two-dimensional GIWAXS patterns of bottom surfaces of perovskite deposited on Me-4PACz and Me:Bi4PACz. (f) XRD spectra of bottom surface of perovskite deposited on Me-4PACz and Me:Bi4PACz. (g) PL spectra of perovskite on Me-4PACz and Me:Bi4PACz.

microscopy (AFM) measurements revealed that the mixed Me:Bi4PACz has a lower roughness (3.79 nm) than that of Me-4PACz (4.66 nm) (Figure 1k,l, Figure S4), indicating a dense, ordered layer favorable for perovskite crystallization.[33,34] The incorporation of Bi4PACz thus creates a uniform coverage with lesser disorder. In the transmittance spectra (Figure S5), ITO/Me-4PACz has a slightly lower transmittance than bare ITO, which can be attributed to the SAM aggregation, whereas Bi4PACz and Me:Bi4PACz exhibit almost no parasitic absorption, consistent with their ordered molecular arrangement and which is beneficial for enhanced short circuit current density (J_{SC}) of the device.[35]

To examine whether Bi4PACz can adopt a face-on adsorption orientation on the substrate surface, the energetic stability of edge-on and face-on adsorption configurations was systematically compared under different surface coverages (Figure S6). The results indicate that under low-coverage conditions the face-on orientation can form relatively more stable adsorption configurations. However, because the face-on configuration occupies a substantially larger lateral area on the substrate surface than the edge-on configuration, intermolecular interactions and steric packing constraints become increasingly pronounced with increasing coverage. Consequently, in the intermediate-to-high-coverage regime, the edge-on orientation exhibits significantly lower adsorption energies than the face-on orientation, demonstrating superior thermodynamic stability and structural feasibility. For a dual-phosphonic-acid molecule, an edge-on adsorption geometry is consistent with an out-of-plane separation of the two phosphonic-acid groups, where one headgroup participates in surface anchoring while the other is positioned farther from the substrate and may remain exposed toward the upper interface and interact with perovskite.

Next, ATR-FTIR measurements were performed on pure Bi4PACz and Bi4PACz+PbI_2 films to investigate the Bi4PACz−perovskite interactions (Figure 2a). The P═O vibration peak at 1149 cm^{-1} indicates the presence of Bi4PACz.[36] In the presence of PbI_2, this peak red shifts to 1141 cm^{-1}, indicating the coordination bond between the phosphate acid and PbI_2, while such peak shifts or interactions are less obvious in the PbI_2+Me-4PACz sample (Figure S7). X-ray photoelectron spectroscopy (XPS) further confirmed this interaction between Bi4PACz and Me-4PACz (Figure 2b). Because of the relationship $E_B = h\nu - E_K - WF$, where E_B is the electron binding energy, $h\nu$ is the photon energy, E_K is the measured kinetic energy, and WF is the spectrometer work function,[37] when the electronic density around an atom increases, the E_K of photoelectrons emitted from core levels

https://doi.org/10.1021/acsenergylett.5c03637
ACS Energy Lett. 2026, 11, 3755−3763

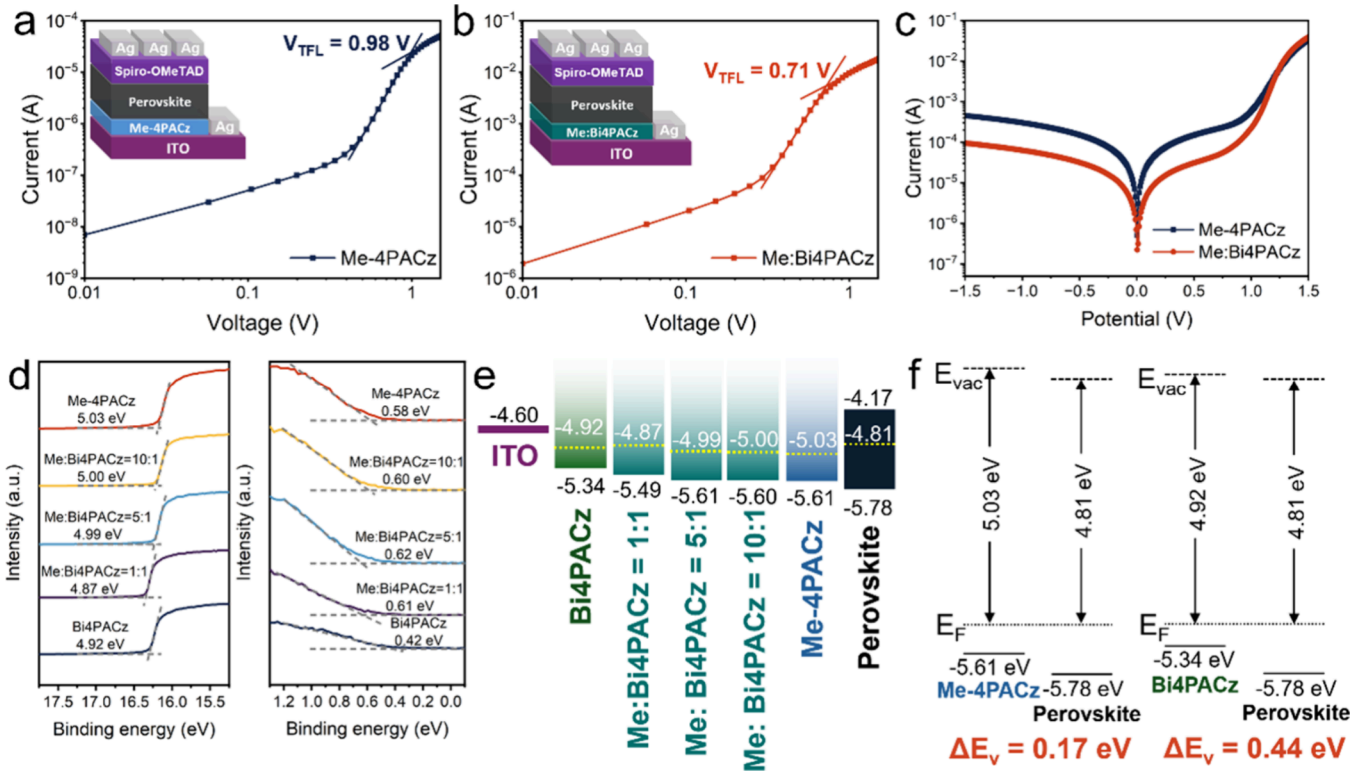

Figure 3. (a, b) Pulsed SCLC measurement of hole-dominated devices based on Me-4PACz and Me:Bi4PACz. (c) Dark current of PSCs based on Me-4PACz and Me:Bi4PACz HTLs. (d) UPS spectra of Me-4PACz, Bi4PACz, and their mixtures with different ratios. (e) Schematic energy-level diagrams of Me-4PACz, Bi4PACz, and Me:Bi4PACz with different mixing ratios. (f) Schematic energy-level diagrams of the Me-4PACz/perovskite and Bi4PACz/perovskite bilayers.

will also increase, leading to a reduced E_B in the XPS spectrum.[38] Accordingly, the Pb 4f peak shift is extensively used to evaluate the interaction between perovskite and functional groups of passivators. After incorporation of Bi4PACz, the Pb 4f peaks of the PbI_2 shift from 143.8 and 139.0 eV to 143.7 and 138.8 eV, respectively. This shift is consistent with the electron-donating nature of Lewis-base oxygen atoms in the phosphonic acid group of Bi4PACz, which can coordinate with unsaturated Pb^{2+} associated with halide-vacancy-related defects in perovskite.[39] Such Pb−O coordination increases the local electron density of defect-related Pb^{2+}, thereby contributing to trap site passivation and enhanced perovskite stability.

To further explore the effect of Me:Bi4PACz on the buried interface, the perovskite bottom surface was exposed via peel-off (Figure S8). AFM characterization for this bottom surface reveals that the perovskite deposited on Me:Bi4PACz shows a smoother buried interface with fewer nanovoids (Figure S9), which is attributed to the improved wettability and stronger HTL−perovskite interaction. Scanning electron microscopy (SEM) images reveal a larger grain size of the perovskite on Me:Bi4PACz (321 nm) near the SAM/perovskite interface, compared with that on Me-4PACz (264 nm) (Figure S10). On the top surface, the perovskite on Me:Bi4PACz also shows a larger average grain size (227 nm versus 182 nm) (Figure S11). In addition, some PbI_2 species are observed at the bottom surface of perovskite on Me-4PACz, mainly located at grain boundaries, while they are largely absent in the Me:Bi4PACz sample.[40] This difference can be attributed to the coordination bond between the Bi4PACz and PbI_2 that inhibits the aggregation of excessive PbI_2 and promotes its conversion into the perovskite phase during crystallization,[33,40−42] as illustrated in Figure 2c. Consequently, Bi4PACz demonstrates effectiveness in suppressing photoinactive PbI_2 at the buried interface and enhancing perovskite crystallinity, which is beneficial for reducing nonradiative recombination, boosting device performance and stability.[43]

Grazing incidence wide-angle X-ray scattering (GIWAXS) measurements (Figure 2d and e) on these buried interfaces also showed a higher intensity of the PbI_2 peak for perovskite on Me-4PACz than on Me:Bi4PACz, while other diffraction features remain similar, indicating comparable crystal orientation. Excess PbI_2 can have adverse effects on device stability, by creating voids and recombination centers under illumination or heat.[44,45] Therefore, Me:Bi4PACz is expected to enhance the stability of the PSCs. Consistent with the GIWAXS results, X-ray diffraction (XRD) of the perovskite bottom surface (Figure 2f) shows a less pronounced PbI_2 peak for the Me:Bi4PACz-based film, indicating a reduced bulk PbI_2. Moreover, the triple cation perovskite exhibits a random crystallite orientation,[46] but the intensity of the (001) peak of the perovskite on Me:Bi4PACz is slightly higher and stronger than that on Me-4PACz, correlated with its larger grain size and improved crystallinity.[47]

To evaluate the possible contribution of physically adsorbed SAM molecules, the spin-coated SAM layers were rinsed with dimethylformamide (DMF) up to three times. Contact angle measurements exhibit no significant difference after rinsing, suggesting that the physically adsorbed SAMs do not play a dominant role in determining the surface properties (Figure S12). Consistently, bottom-surface SEM (Figure S13) and GIWAXS (Figure S14) characterizations of perovskite films

https://doi.org/10.1021/acsenergylett.5c03637
ACS Energy Lett. 2026, 11, 3755−3763

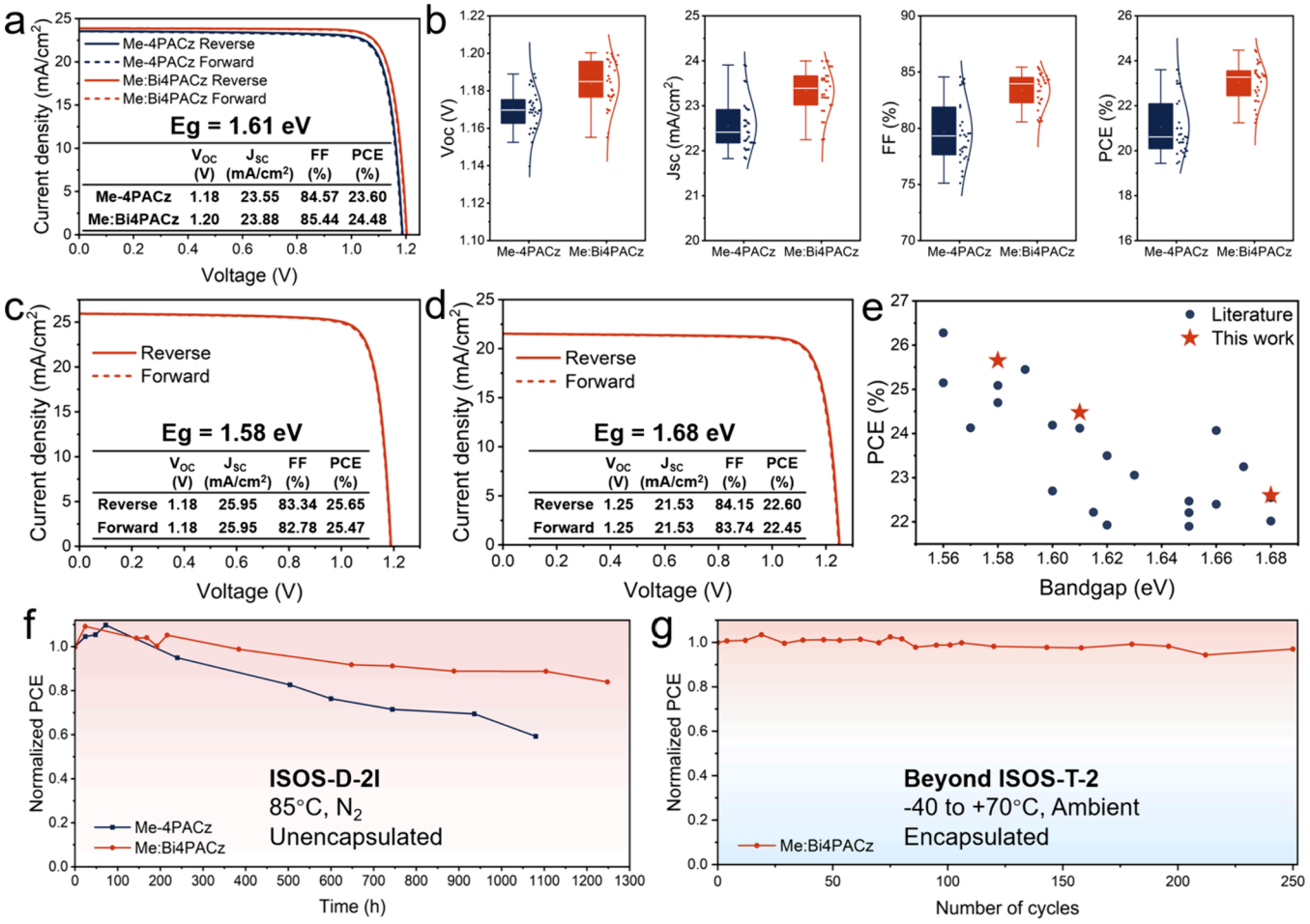

Figure 4. (a) $J-V$ curves of Me-4PACz and Me:Bi4PACz devices with a 1.61 eV bandgap absorption layer. (b) Statistics of V_{OC}, J_{SC}, FF, and PCE of Me-4PACz and Me:Bi4PACz PSCs based on 26 devices. (c, d) $J-V$ curves of the Me:Bi4PACz device with a (c) 1.55 eV and (d) 1.68 eV bandgap absorption layer. (e) PCE comparison of PSCs with bandgaps between 1.56 and 1.68 eV. The comprehensive photovoltaic performance of these reported devices is outlined in Table S2, Supporting Information. (f) Thermal stability of unencapsulated PSCs at 85 °C in a N_2 environment. (g) Thermal cycling stability of encapsulated PSCs between −40 and +70 °C.

deposited on SAM layers with a single DMF rinse show interfacial crystallization behavior comparable to that observed without rinsing. These results suggest that the key interfacial effects are primarily governed by the anchored SAMs, instead of physically adsorbed molecules.

The Me:Bi4PACz HTL can thus improve not only the crystal quality of the perovskite but also the uniformity of the perovskite bottom surface. As shown in the photoluminescence (PL) mapping images (Figure S15), the perovskite film on Me:Bi4PACz exhibited a more homogeneous and intense PL signal across the scanned area compared to that on Me-4PACz, evidencing an improved bottom surface uniformity with less defects. Meanwhile, the steady-state PL (Figure 2g) from the bottom surface of perovskite films reveals that the perovskite on Me:Bi4PACz has an enhanced PL intensity compared with that on Me-4PACz, further indicating the improved quality of the perovskite bottom surface and reduced nonradiative recombination.[6,48] These results are consistent with the time-resolved PL (TRPL) measurement (Figure S16), where the perovskite on Me:Bi4PACz shows a carrier lifetime longer than that on Me-4PACz.

To investigate the effect of Me:Bi4PACz on charge trap suppression, we fabricated hole-dominated devices (ITO/SAM/perovskite/spiro-OMeTAD/Ag) to conduct pulsed space charge limited current (SCLC) analysis under dark conditions (Supplementary Note 2). As shown in Figure 3a and b, the Me:Bi4PACz device exhibits a lower V_{TFL} (0.71 V) than the Me-4PACz device (V_{TFL} ~ 0.98 V), and thus a lower hole trap density (n_t is 7.70×10^{15} cm^{-3} and 1.06×10^{16} cm^{-3} for the Me:Bi4PACz and Me-4PACz device, respectively). The reduced trap density in the mixed system indicates suppressed nonradiative recombination and enhanced perovskite crystal quality. In the dark current curves, the Me:Bi4PACz PSC device exhibits a lower leakage current (Figure 3c), indicating an increased shunt resistance and less charge recombination.[33,49]

To optimize the mixing ratio of Me-4PACz and Bi4PACz, PSCs with various mixing ratios (10:1 to 0:1) were fabricated (Figure S17). The PCE increased from 10:1 to 5:1 due to the beneficial effect of Bi4PACz discussed above, but decreased as the Bi4PACz proportion further increased. Devices using pure Bi4PACz (0:1) show low efficiency, mainly due to the inferior open circuit voltage (V_{OC}) and fill factor (FF).

Ultraviolet photoelectron spectroscopy (UPS) was employed to investigate this (Figure 3d and e, Figure S18), which reveals that the work function (WF) and highest occupied molecular orbital (HOMO) of Me-4PACz are deeper than Bi4PACz, resulting in a larger energy-level offset between

https://doi.org/10.1021/acsenergylett.5c03637
ACS Energy Lett. 2026, 11, 3755−3763

the HOMO of HTL and the valence band maximum (VBM) of perovskite (ΔE_V = 0.44 eV) at the Bi4PACz/perovskite interface compared with 0.17 eV for Me-4PACz (Figure 3f), indicating that pure Bi4PACz is unfavorable for hole transfer in the photovoltaic device.[50] Transient photocurrent (TPC) measurement was also performed to evaluate the charge transfer behavior (Figure S19). The device employing Bi4PACz exhibits slightly slower TPC decay compared to the Me-4PACz device, indicating hindered charge transfer dynamics. This slower current response is consistent with the larger energy-level offset between the perovskite VBM and the Bi4PACz HOMO level, which may impose an additional barrier for hole transfer across the interface. When Me-4PACz is mixed with Bi4PACz, the WFs and HOMOs lie between those of the pure components, becoming shallower with the proportion growth of Bi4PACz (Figure 3d and e). This evolution does not strictly follow a linear relationship with the mixing ratio, indicating that the mixed SAM does not behave as a simple superposition of two independent dipole layers. Instead, mixing two different SAMs modifies the local interfacial electronic environment, leading to an effective or joint density of states (DOS), rather than a rigid shift of a single DOS. As in mixed organic semiconductors, the coexistence of two electronic species can redistribute state occupation, resulting in a nonlinear evolution of the effective Fermi level, vacuum-level shift, and thus the WF and band alignment on the mixing ratio.[51] For 5:1 and 10:1, the energy levels of Me:Bi4PACz remain close to those of pure Me-4PACz, maintaining favorable energy alignment with the perovskite. Balancing efficient interfacial passivation and optimal energy-level alignment, the 5:1 ratio yielded the highest average PCE and was selected as the optimal composition.

Based on the results obtained above, we fabricated devices with an architecture of ITO/SAM/$Cs_{0.05}(FA_{0.85}MA_{0.15})_{0.95}Pb(I_{0.85}Br_{0.15})_3$/propane-1,3-diammonium iodide ($PDAI_2$)[52]/C_{60}/bathocuproine (BCP)/Ag to evaluate the Me:Bi4PACz mixed SAM, where the triple cation perovskite has a bandgap of 1.61 eV (Figure S20), and the active area is 0.05 cm^2. According to the photovoltaic performance shown in Figure 4a and Table S1, the target Me:Bi4PACz device achieved a champion PCE of 24.48% (V_{OC} = 1.20 V, J_{SC} = 23.88 mA cm^{-2}, FF = 85.44%), with negligible hysteresis, outperforming Me-4PACz devices (PCE = 23.60%). Statistical results (Figure 4b and Table S2) confirm a higher average PCE and narrower distribution of Me:Bi4PACz devices (23.03% ± 0.85 SD) than Me-4PACz devices (21.04% ± 1.25 SD), which can be attributed to the enhanced homogenization of SAM and improved buried interface quality of perovskite. The J_{SC} of the device is consistent with the integrated J_{SC} from the external quantum efficiency (EQE) result (23.1 mA cm^{-2}, Figure S21). We also fabricated PSCs on the DMF-rinsed SAM layers, which exhibit performance trends consistent with those obtained without rinsing. Both the champion PCE and the statistical distribution (Figure S22) remained comparable, underscoring that the performance enhancement is predominantly associated with the anchored SAMs rather than physically adsorbed molecules.

Using the same approach, PSCs based on 1.58 eV $Cs_{0.05}(FA_{0.95}MA_{0.05})_{0.95}Pb(I_{0.95}Br_{0.05})_3$ perovskite (Figure S23) and 1.68 eV $Cs_{0.05}FA_{0.80}MA_{0.15}Pb(I_{0.75}Br_{0.25})_3$ perovskite (Figure S24) were fabricated, which delivered champion PCEs of 25.65% and 22.60%, respectively (Figure 4c and d), exhibiting the wide applicability of this mixed SAM strategy. Compared with reported PSCs across bandgaps of 1.56−1.68 eV (Figure 4e, Table S3), our devices show outstanding PCE relative to other devices with comparable bandgaps. In particular, our 1.61 eV PSC demonstrates, to the best of our knowledge, the highest reported efficiency among PSCs with bandgaps exceeding 1.6 eV (Table S3). We also explored the potential of large-area devices by fabricating a 1.61 eV PSC with an active area of 1 cm^2 (Figure S25). The improved wettability of HTL leads to a pinhole-free perovskite film, and the device achieved a PCE of 21.8% (V_{OC} = 1.21 V, J_{SC} = 23.70 mA/cm^2, FF = 76.04%).

Finally, the long-term stability of the PSCs based on the 1.61 eV $Cs_{0.05}(FA_{0.85}MA_{0.15})_{0.95}Pb(I_{0.85}Br_{0.15})_3$ perovskite was assessed in different environments. Under continuous heating at 85 °C in N_2, the unencapsulated Me:Bi4PACz PSC maintained 84% of its initial PCE after ∼1200 h, outperforming the Me-4PACz device, which only retained 59% after ∼1000 h (Figure 4f). To further evaluate the robustness of the device under space-relevant conditions, thermal cycling from −40 °C to +70 °C, with a rate of temperature variation of 5 °C min^{-1} and a 5 min dwell at each temperature extreme, was performed (Figure S26). The Me:Bi4PACz PSC maintained 97% of the initial PCE after 250 thermal cycles (Figure 4g), highlighting its excellent thermal cycling stability and potential for space-related applications. A maximum power point tracking (MPPT) test was also performed for the encapsulated devices in air at ∼40 °C (∼25% relative humidity) under white LED illumination (Figure S27), where the Me:Bi4PACz device exhibits an improved operational stability compared to the Me-4PACz device. Overall, Me:Bi4PACz endows the devices with remarkable thermal and cycling stability, ensuring reliable operation under prolonged stress conditions.

We also stored the $Cs_{0.05}(FA_{0.85}MA_{0.15})_{0.95}Pb(I_{0.85}Br_{0.15})_3$ perovskite films on Me-4PACz and Me:Bi4PACz at 85 °C in N_2 for ∼170 h. According to the cross-section SEM images of these perovskite films (Figure S28), after thermal aging, there are bright grains embedded in the perovskite layer deposited on Me-4PACz, which can be assigned to PbI_2 domains,[41,53] while the presence of these bright PbI_2-related features is much less evident in the perovskite film on Me:Bi4PACz. This phenomenon can also be supported by the XRD spectra of perovskite films before and after aging (Figure S29). After thermal aging, the perovskite on Me-4PACz shows a significantly enhanced intensity of the PbI_2 peak at 12.5° compared to before aging, which indicates more pronounced degradation after thermal aging. By contrast, the perovskite on Me:Bi4PACz shows a lower relative intensity of PbI_2 and a higher (100) peak at 14.1° after aging. PbI_2 is known as the perovskite decomposition product due to loss of organic components, which acts as evidence of degradation.[54−56] According to the results in previous studies, the Bi4PACz forms robust coordination bonds with Pb^{2+}, passivating trap states and increasing the activation barrier for A-site and halide vacancy formation, suppressing PbI_2 segregation during crystallization or thermal stress.[52,57] Meanwhile, the mixed SAM improves perovskite crystal quality, resulting in fewer degradation-sensitive hotspots.[58] Therefore, PbI_2 reformation and interfacial structural destruction are effectively mitigated during thermal aging. These results highlight the crucial role of buried-interface engineering in suppressing thermal degradation pathways and enhancing the device temperature stability.

https://doi.org/10.1021/acsenergylett.5c03637
ACS Energy Lett. 2026, 11, 3755−3763

In conclusion, this work introduces a co-self-assembly strategy using a mixed SAM composed of Me-4PACz and Bi4PACz to ameliorate the buried interface quality of perovskite and boost device performance for p-i-n PSCs. This Me:Bi4PACz mixed SAM effectively solves the hydrophobicity and coverage issues of Me-4PACz, while maintaining a simple, interlayer-free fabrication process. The interaction between Bi4PACz and the perovskite enables effective defect passivation, suppresses PbI_2 aggregation, and enhances perovskite film uniformity, thereby reducing recombination losses at the buried interface. The improvement in buried interface quality leads to an outstanding photovoltaic performance of the PSCs with a 1.61 eV bandgap triple cation perovskite absorption layer, achieving a champion PCE of 24.48% and excellent long-term stability under thermal and thermal cycling conditions. The high reproducibility and broad applicability of this HTL engineering strategy highlight its promise for scalable, high-efficiency, and stable PSCs and potential use in space-related applications.

■ ASSOCIATED CONTENT

Supporting Information

The Supporting Information is available free of charge at https://pubs.acs.org/doi/10.1021/acsenergylett.5c03637.

Experimental details including materials, device fabrication, and characterizations; DFT computation methods; pulsed SCLC measurement and calculation; contact angle images; DFT results; ATR-FTIR spectra; AFM images; transmittance spectra; schematic of peel-off process; SEM images and grain size statistics; contact angle graphs; GIWAXS graphs; PL mapping spectra; TRPL spectra; box plots of photovoltaic parameters; UPS spectra; TPC plots; UV−vis absorption and Tauc plots; $J-V$ curve of 1.61 eV 1 cm^2 PSC; temperature−time curve of the thermal cycling test; MPPT plots; cross-section SEM and XRD of perovskite films; and tables of champion and statistics of device performance parameters of our 1.61 eV PSCs and reported 1.56−1.68 eV PSCs in the literature (PDF)

■ AUTHOR INFORMATION

Corresponding Authors

Nripan Mathews − *Energy Research Institute @ NTU (ERI@N), Nanyang Technological University, Singapore 637553, Singapore; School of Materials Science and Engineering, Nanyang Technological University, Singapore 639798, Singapore;* orcid.org/0000-0001-5234-0822; Email: Nripan@ntu.edu.sg

Wei Lin Leong − *Energy Research Institute @ NTU (ERI@N), Nanyang Technological University, Singapore 637553, Singapore; School of Electrical and Electronic Engineering, Nanyang Technological University, Singapore 639798, Singapore;* orcid.org/0000-0002-1402-0083; Email: wlleong@ntu.edu.sg

Authors

Haonan Sun − *Interdisciplinary Graduate Programme (IGP), Graduate College, Nanyang Technological University, Singapore 637460, Singapore; Energy Research Institute @ NTU (ERI@N), Nanyang Technological University, Singapore 637553, Singapore*

Guibin Shen − *School of Electrical and Electronic Engineering, Nanyang Technological University, Singapore 639798, Singapore*

Huei Min Chua − *School of Electrical and Electronic Engineering, Nanyang Technological University, Singapore 639798, Singapore;* orcid.org/0000-0001-6112-9594

Darrell Jun Jie Tay − *School of Materials Science and Engineering, Nanyang Technological University, Singapore 639798, Singapore*

Yuanjie Su − *Beijing National Laboratory for Condensed Matter Physics, Institute of Physics, Chinese Academy of Sciences, Beijing 100190, China; School of Physics, University of Chinese Academy of Sciences, Beijing 100049, China*

Yahong Pu − *Beijing National Laboratory for Condensed Matter Physics, Institute of Physics, Chinese Academy of Sciences, Beijing 100190, China; School of Physics, University of Chinese Academy of Sciences, Beijing 100049, China*

Yanju Wang − *School of Electrical and Electronic Engineering, Nanyang Technological University, Singapore 639798, Singapore*

Yeow Boon Tay − *School of Materials Science and Engineering, Nanyang Technological University, Singapore 639798, Singapore*

Hongkang Fu − *Interdisciplinary Graduate Programme (IGP), Graduate College, Nanyang Technological University, Singapore 637460, Singapore; School of Electrical and Electronic Engineering, Nanyang Technological University, Singapore 639798, Singapore*

Subodh G. Mhaisalkar − *Energy Research Institute @ NTU (ERI@N), Nanyang Technological University, Singapore 637553, Singapore; School of Materials Science and Engineering, Nanyang Technological University, Singapore 639798, Singapore;* orcid.org/0000-0002-9895-2426

Shixuan Du − *Beijing National Laboratory for Condensed Matter Physics, Institute of Physics, Chinese Academy of Sciences, Beijing 100190, China; School of Physics, University of Chinese Academy of Sciences, Beijing 100049, China;* orcid.org/0000-0001-9323-1307

Complete contact information is available at: https://pubs.acs.org/10.1021/acsenergylett.5c03637

Author Contributions

[&]H.S. and G.S. contributed equally to this work.

Notes

The authors declare no competing financial interest.

■ ACKNOWLEDGMENTS

This research was supported by the Economic Development Board (EDB) Office for Space Technology and Industry (OSTIn) under the Space Technology Development Programme (S22-02002-STDP) and National Research Foundation (NRF), Singapore, under its Competitive Research Program (CRP) (NRF-CRP25-2020-002).

■ REFERENCES

(1) Chen, P.; Xiao, Y.; Li, S.; Jia, X.; Luo, D.; Zhang, W.; Snaith, H. J.; Gong, Q.; Zhu, R. The Promise and Challenges of Inverted Perovskite Solar Cells. *Chem. Rev.* **2024**, *124* (19), 10623−10700.

(2) *Best Research-Cell Efficiency Chart | Photovoltaic Research | NREL.* https://www.nrel.gov/pv/cell-efficiency.html (accessed 2025−03−03).

(3) Cao, F.; Wang, M.; Li, L. Pushing the Certified Efficiency of Inverted Perovskite Solar Cells beyond 24%: A Review. *Review of Materials Research* **2025**, *1* (2), No. 100020.
(4) Yi, Z.; Li, X.; Xiong, Y.; Shen, G.; Zhang, W.; Huang, Y.; Jiang, Q.; Ng, X. R.; Luo, Y.; Zheng, J.; Leong, W. L.; Fu, F.; Bu, T.; Yang, J. Self-Assembled Monolayers (SAMs) in Inverted Perovskite Solar Cells and Their Tandem Photovoltaics Application. *Interdisciplinary Materials* **2024**, *3* (2), 203−244.
(5) Levine, I.; Al-Ashouri, A.; Musiienko, A.; Hempel, H.; Magomedov, A.; Drevilkauskaite, A.; Getautis, V.; Menzel, D.; Hinrichs, K.; Unold, T.; Albrecht, S.; Dittrich, T. Charge Transfer Rates and Electron Trapping at Buried Interfaces of Perovskite Solar Cells. *Joule* **2021**, *5* (11), 2915−2933.
(6) Park, S. M.; Wei, M.; Lempesis, N.; Yu, W.; Hossain, T.; Agosta, L.; Carnevali, V.; Atapattu, H. R.; Serles, P.; Eickemeyer, F. T.; Shin, H.; Vafaie, M.; Choi, D.; Darabi, K.; Jung, E. D.; Yang, Y.; Kim, D. B.; Zakeeruddin, S. M.; Chen, B.; Amassian, A.; Filleter, T.; Kanatzidis, M. G.; Graham, K. R.; Xiao, L.; Rothlisberger, U.; Grätzel, M.; Sargent, E. H. Low-Loss Contacts on Textured Substrates for Inverted Perovskite Solar Cells. *Nature* **2023**, *624* (7991), 289−294.
(7) Yu, S.; Xiong, Z.; Zhou, H.; Zhang, Q.; Wang, Z.; Ma, F.; Qu, Z.; Zhao, Y.; Chu, X.; Zhang, X.; You, J. Homogenized NiOx Nanoparticles for Improved Hole Transport in Inverted Perovskite Solar Cells. *Science* **2023**, *382* (6677), 1399−1404.
(8) Hossain, K.; Kulkarni, A.; Bothra, U.; Klingebiel, B.; Kirchartz, T.; Saliba, M.; Kabra, D. Resolving the Hydrophobicity of the Me-4PACz Hole Transport Layer for Inverted Perovskite Solar Cells with Efficiency > 20%. *ACS Energy Lett.* **2023**, *8* (9), 3860−3867.
(9) Pitaro, M.; Alonso, J. E. S.; Di Mario, L.; Romero, D. G.; Tran, K.; Kardula, J.; Zaharia, T.; Johansson, M. B.; Johansson, E. M. J.; Chiechi, R. C.; Loi, M. A. Tuning the Surface Energy of Hole Transport Layers Based on Carbazole Self-Assembled Monolayers for Highly Efficient Sn/Pb Perovskite Solar Cells. *Adv. Funct. Mater.* **2024**, *34* (50), 2306571.
(10) Al-Ashouri, A.; Marčinskas, M.; Kasparavičius, E.; Malinauskas, T.; Palmstrom, A.; Getautis, V.; Albrecht, S.; McGehee, M. D.; Magomedov, A. Wettability Improvement of a Carbazole-Based Hole-Selective Monolayer for Reproducible Perovskite Solar Cells. *ACS Energy Lett.* **2023**, *8* (2), 898−900.
(11) Liu, S.; Li, J.; Xiao, W.; Chen, R.; Sun, Z.; Zhang, Y.; Lei, X.; Hu, S.; Kober-Czerny, M.; Wang, J.; Ren, F.; Zhou, Q.; Raza, H.; Gao, Y.; Ji, Y.; Li, S.; Li, H.; Qiu, L.; Huang, W.; Zhao, Y.; Xu, B.; Liu, Z.; Snaith, H. J.; Park, N.-G.; Chen, W. Buried Interface Molecular Hybrid for Inverted Perovskite Solar Cells. *Nature* **2024**, *632* (8025), 536−542.
(12) He, X.; Chen, H.; Yang, J.; Wang, T.; Pu, X.; Feng, G.; Jia, S.; Bai, Y.; Zhou, Z.; Cao, Q.; Li, X. Enhancing Hole Transport Uniformity for Efficient Inverted Perovskite Solar Cells through Optimizing Buried Interface Contacts and Suppressing Interface Recombination. *Angew. Chem.* **2024**, *136* (52), No. e202412601.
(13) Li, C.; Wang, X.; Bi, E.; Jiang, F.; Park, S. M.; Li, Y.; Chen, L.; Wang, Z.; Zeng, L.; Chen, H.; Liu, Y.; Grice, C. R.; Abudulimu, A.; Chung, J.; Xian, Y.; Zhu, T.; Lai, H.; Chen, B.; Ellingson, R. J.; Fu, F.; Ginger, D. S.; Song, Z.; Sargent, E. H.; Yan, Y. Rational Design of Lewis Base Molecules for Stable and Efficient Inverted Perovskite Solar Cells. *Science* **2023**, *379* (6633), 690−694.
(14) Perera, W. H. K.; Masteghin, M. G.; Shim, H.; Davies, J. D.; Ryan, J. L.; Hinder, S. J.; Yun, J. S.; Zhang, W.; Jayawardena, K. D. G. I.; Silva, S. R. P. Modification of Hydrophobic Self-Assembled Monolayers with Nanoparticles for Improved Wettability and Enhanced Carrier Lifetimes Over Large Areas in Perovskite Solar Cells. *Solar RRL* **2023**, *7* (17), 2300388.
(15) Liu, X.; Li, B.; Han, M.; Zhang, X.; Chen, J.; Dai, S. Research Progress of Self-assembled Hole-transporting Monolayers in Inverted Perovskite Solar Cells. *Acta Chimica Sinica* **2024**, *82* (3), 348.
(16) Phung, N.; Verheijen, M.; Todinova, A.; Datta, K.; Verhage, M.; Al-Ashouri, A.; Köbler, H.; Li, X.; Abate, A.; Albrecht, S.; Creatore, M. Enhanced Self-Assembled Monolayer Surface Coverage by ALD NiO in p-i-n Perovskite Solar Cells. *ACS Appl. Mater. Interfaces* **2022**, *14* (1), 2166−2176.
(17) Chen, J.; Wang, X.; Wang, T.; Li, J.; Chia, H. Y.; Liang, H.; Xi, S.; Liu, S.; Guo, X.; Guo, R.; Jia, Z.; Yin, X.; Zhou, Q.; Wang, Y.; Shi, Z.; Zhou, H.; Lai, D.; Zhang, M.; Xing, Z.; Leow, W. R.; Yan, W.; Hou, Y. Determining the Bonding−Degradation Trade-off at Heterointerfaces for Increased Efficiency and Stability of Perovskite Solar Cells. *Nat. Energy* **2024**, *10* (2), 181−190.
(18) Yan, N.; Fang, Z.; Dai, Z.; Feng, J.; Liu, S. F. Buried Interface-The Key Issues for High Performance Inverted Perovskite Solar Cells. *Adv. Funct. Mater.* **2024**, *34* (22), 2314039.
(19) Wang, Q.; Chueh, C.-C.; Zhao, T.; Cheng, J.; Eslamian, M.; Choy, W. C. H.; Jen, A. K.-Y. Effects of Self-Assembled Monolayer Modification of Nickel Oxide Nanoparticles Layer on the Performance and Application of Inverted Perovskite Solar Cells. *ChemSusChem* **2017**, *10* (19), 3794−3803.
(20) Mangalam, J.; Rath, T.; Weber, S.; Kunert, B.; Dimopoulos, T.; Fian, A.; Trimmel, G. Modification of NiOx Hole Transport Layers with 4-Bromobenzylphosphonic Acid and Its Influence on the Performance of Lead Halide Perovskite Solar Cells. *J. Mater. Sci: Mater. Electron* **2019**, *30* (10), 9602−9611.
(21) Boyd, C. C.; Shallcross, R. C.; Moot, T.; Kerner, R.; Bertoluzzi, L.; Onno, A.; Kavadiya, S.; Chosy, C.; Wolf, E. J.; Werner, J.; Raiford, J. A.; Paula, C. de; Palmstrom, A. F.; Yu, Z. J.; Berry, J. J.; Bent, S. F.; Holman, Z. C.; Luther, J. M.; Ratcliff, E. L.; Armstrong, N. R.; McGehee, M. D. Overcoming Redox Reactions at Perovskite-Nickel Oxide Interfaces to Boost Voltages in Perovskite Solar Cells. *Joule* **2020**, *4* (8), 1759−1775.
(22) Zhang, J.; Yang, J.; Dai, R.; Sheng, W.; Su, Y.; Zhong, Y.; Li, X.; Tan, L.; Chen, Y. Elimination of Interfacial Lattice Mismatch and Detrimental Reaction by Self-Assembled Layer Dual-Passivation for Efficient and Stable Inverted Perovskite Solar Cells. *Adv. Energy Mater.* **2022**, *12* (18), 2103674.
(23) Zhang, H.; Park, N.-G. Progress and Issues in P-i-n Type Perovskite Solar Cells. *DeCarbon* **2024**, *3*, No. 100025.
(24) Paniagua, S. A.; Giordano, A. J.; Smith, O. L.; Barlow, S.; Li, H.; Armstrong, N. R.; Pemberton, J. E.; Brédas, J.-L.; Ginger, D.; Marder, S. R. Phosphonic Acids for Interfacial Engineering of Transparent Conductive Oxides. *Chem. Rev.* **2016**, *116* (12), 7117−7158.
(25) Ren, Z.; Cui, Z.; Shi, X.; Wang, L.; Dou, Y.; Wang, F.; Lin, H.; Yan, H.; Chen, S. Poly(Carbazole Phosphonic Acid) as a Versatile Hole-Transporting Material for p-i-n Perovskite Solar Cells and Modules. *Joule* **2023**, *7* (12), 2894−2904.
(26) Kulkarni, A.; Sarkar, R.; Akel, S.; Häser, M.; Klingebiel, B.; Wuttig, M.; Wiegand, S.; Chakraborty, S.; Saliba, M.; Kirchartz, T. A Universal Strategy of Perovskite Ink - Substrate Interaction to Overcome the Poor Wettability of a Self-Assembled Monolayer for Reproducible Perovskite Solar Cells. *Adv. Funct. Mater.* **2023**, *33* (47), 2305812.
(27) Wang, R.; Liu, X.; Yan, S.; Meng, N.; Zhao, X.; Chen, Y.; Li, H.; Qaid, S. M. H.; Yang, S.; Yuan, M.; He, T. Efficient Wide-Bandgap Perovskite Photovoltaics with Homogeneous Halogen-Phase Distribution. *Nat. Commun.* **2024**, *15* (1), 8899.
(28) Ulman, A. Formation and Structure of Self-Assembled Monolayers. *Chem. Rev.* **1996**, *96* (4), 1533−1554.
(29) Liu, M.; Bi, L.; Jiang, W.; Zeng, Z.; Tsang, S.-W.; Lin, F. R.; Jen, A. K.-Y. Compact Hole-Selective Self-Assembled Monolayers Enabled by Disassembling Micelles in Solution for Efficient Perovskite Solar Cells. *Adv. Mater.* **2023**, *35* (46), 2304415.
(30) Fariya, M.; Jain, A.; Dhawan, V.; Shah, S.; Nagarsenker, M. S. Bolaamphiphiles: A Pharmaceutical Review. *Adv. Pharm. Bull.* **2014**, *4*, 483−491.
(31) Dhasaiyan, P.; Prasad, B. L. V. Self-Assembly of Bolaamphiphilic Molecules. *Chem. Rec.* **2017**, *17* (6), 597−610.
(32) Li, C.; Zhang, Z.; Zhang, H.; Yan, W.; Li, Y.; Liang, L.; Yu, W.; Yu, X.; Wang, Y.; Yang, Y.; Nazeeruddin, M. K.; Gao, P. Fully Aromatic Self-Assembled Hole-Selective Layer toward Efficient Inverted Wide-Bandgap Perovskite Solar Cells with Ultraviolet Resistance. *Angew. Chem.* **2024**, *136* (1), No. e202315281.

https://doi.org/10.1021/acsenergylett.5c03637
ACS Energy Lett. 2026, 11, 3755−3763

(33) Li, D.; Lian, Q.; Du, T.; Ma, R.; Liu, H.; Liang, Q.; Han, Y.; Mi, G.; Peng, O.; Zhang, G.; Peng, W.; Xu, B.; Lu, X.; Liu, K.; Yin, J.; Ren, Z.; Li, G.; Cheng, C. Co-Adsorbed Self-Assembled Monolayer Enables High-Performance Perovskite and Organic Solar Cells. *Nat. Commun.* **2024**, *15* (1), 7605.
(34) Qu, G.; Cai, S.; Qiao, Y.; Wang, D.; Gong, S.; Khan, D.; Wang, Y.; Jiang, K.; Chen, Q.; Zhang, L.; Wang, Y.-G.; Chen, X.; Jen, A. K.-Y.; Xu, Z.-X. Conjugated Linker-Boosted Self-Assembled Monolayer Molecule for Inverted Perovskite Solar Cells. *Joule* **2024**, *8* (7), 2123−2134.
(35) Li, E.; Bi, E.; Wu, Y.; Zhang, W.; Li, L.; Chen, H.; Han, L.; Tian, H.; Zhu, W.-H. Synergistic Coassembly of Highly Wettable and Uniform Hole-Extraction Monolayers for Scaling-up Perovskite Solar Cells. *Adv. Funct. Mater.* **2020**, *30* (7), 1909509.
(36) Al-Ashouri, A.; Magomedov, A.; Roß, M.; Jošt, M.; Talaikis, M.; Chistiakova, G.; Bertram, T.; Márquez, J. A.; Köhnen, E.; Kasparavičius, E.; Levcenco, S.; Gil-Escrig, L.; Hages, C. J.; Schlatmann, R.; Rech, B.; Malinauskas, T.; Unold, T.; Kaufmann, C. A.; Korte, L.; Niaura, G.; Getautis, V.; Albrecht, S. Conformal Monolayer Contacts with Lossless Interfaces for Perovskite Single Junction and Monolithic Tandem Solar Cells. *Energy Environ. Sci.* **2019**, *12* (11), 3356−3369.
(37) Einstein, A. Über Einen Die Erzeugung Und Verwandlung Des Lichtes Betreffenden Heuristischen Gesichtspunkt. *Annalen der Physik* **1905**, *322* (6), 132−148.
(38) Siegbahn, K.; Nordling, C. L. A.; Fahlman, A. *ESCA: Atomic, Molecular and Solid State Structure Studied by Means of Electron Spectroscopy*; Nova acta Regiae Societatis Scientiarum Upsaliensis; Ser. 4, Vol. 20; Almqvist & Wiksells Boktryckeri AB: Uppsala, 1967.
(39) Yao, Q.; Xue, Q.; Li, Z.; Zhang, K.; Zhang, T.; Li, N.; Yang, S.; Brabec, C. J.; Yip, H.-L.; Cao, Y. Graded 2D/3D Perovskite Heterostructure for Efficient and Operationally Stable MA-Free Perovskite Solar Cells. *Adv. Mater.* **2020**, *32* (26), 2000571.
(40) Zhu, B.; Li, B.; Ding, G.; Jin, Z.; Xu, Y.; Yang, J.; Wang, Y.; Zhang, Q.; Rui, Y. Eliminating Voids and Residual PbI2 beneath a Perovskite Film via Buried Interface Modification for Efficient Solar Cells. *ACS Appl. Mater. Interfaces* **2024**, *16* (22), 28560−28569.
(41) Gao, Y.; Ren, F.; Sun, D.; Li, S.; Zheng, G.; Wang, J.; Raza, H.; Chen, R.; Wang, H.; Liu, S.; Yu, P.; Meng, X.; He, J.; Zhou, J.; Hu, X.; Zhang, Z.; Qiu, L.; Chen, W.; Liu, Z. Elimination of Unstable Residual Lead Iodide near the Buried Interface for the Stability Improvement of Perovskite Solar Cells. *Energy Environ. Sci.* **2023**, *16* (5), 2295−2303.
(42) Cho, S.-H.; Cho, S. C.; Chang, S.-J.; Lee, S. U.; Park, N.-G. Solution-Phase PbI2 Coordination Controls Perovskite Film Formation and Photovoltaic Performance. *ACS Energy Lett.* **2025**, *10* (8), 3931−3940.
(43) Jiang, W.; Liu, M.; Li, Y.; Lin, F. R.; Jen, A. K.-Y. Rational Molecular Design of Multifunctional Self-Assembled Monolayers for Efficient Hole Selection and Buried Interface Passivation in Inverted Perovskite Solar Cells. *Chem. Sci.* **2024**, *15* (8), 2778−2785.
(44) Roose, B.; Dey, K.; Chiang, Y.-H.; Friend, R. H.; Stranks, S. D. Critical Assessment of the Use of Excess Lead Iodide in Lead Halide Perovskite Solar Cells. *J. Phys. Chem. Lett.* **2020**, *11* (16), 6505−6512.
(45) Jiang, W.; Hu, Y.; Li, F.; Lin, F. R.; Jen, A. K.-Y. Hole-Selective Contact with Molecularly Tailorable Reactivity for Passivating High-Performing Inverted Perovskite Solar Cells. *CCS. Chemistry* **2024**, *6* (7), 1654−1661.
(46) Zhang, S.; Ye, F.; Wang, X.; Chen, R.; Zhang, H.; Zhan, L.; Jiang, X.; Li, Y.; Ji, X.; Liu, S.; Yu, M.; Yu, F.; Zhang, Y.; Wu, R.; Liu, Z.; Ning, Z.; Neher, D.; Han, L.; Lin, Y.; Tian, H.; Chen, W.; Stolterfoht, M.; Zhang, L.; Zhu, W.-H.; Wu, Y. Minimizing Buried Interfacial Defects for Efficient Inverted Perovskite Solar Cells. *Science* **2023**, *380* (6643), 404−409.
(47) Wang, Z.; Han, Z.; Chu, X.; Zhou, H.; Yu, S.; Zhang, Q.; Xiong, Z.; Qu, Z.; Tian, H.; Wang, W.; Wan, F.; Yuan, Y.; Lin, Y.; Yang, Y.; Zhang, X.; Jiang, Q.; You, J. Regulation of Wide Bandgap Perovskite by Rubidium Thiocyanate for Efficient Silicon/Perovskite Tandem Solar Cells. *Adv. Mater.* **2024**, *36* (50), 2407681.
(48) Zhou, B.; Shang, C.; Wang, C.; Qu, D.; Qiao, J.; Zhang, X.; Zhao, W.; Han, R.; Dong, S.; Xue, Y.; Ke, Y.; Ye, F.; Yang, X.; Tu, Y.; Huang, W. Strain Engineering and Halogen Compensation of Buried Interface in Polycrystalline Halide Perovskites. *Research* **2024**, *7*, No. 0309.
(49) Zhi, C.; Li, C.; Wan, Z.; Liu, C.; Jiang, Z.; Zunair, H.; Du, L.; Zhang, S.; Li, Z.; Shi, J.; Li, Z. Boosting Efficiency and UV Resistance in Perovskite Solar Cells via Sunscreen Ingredient Octinoxate. *Adv. Funct. Mater.* **2024**, *34* (39), 2403321.
(50) Kim, D.-H.; Lee, H.-J.; Lee, S.-H.; Kang, Y.-J.; Kwon, S.-N.; Kim, D.-H.; Na, S.-I. Mixed Self-Assembled Hole-Transport Monolayer Enables Simultaneous Improvement of Efficiency and Stability of Perovskite Solar Cells. *Solar RRL* **2024**, *8* (9), 2400067.
(51) Jain, N.; Saxena, R.; Vaidya, S.; Huang, W.; Welford, A.; McNeill, C. R.; Kabra, D. Light Induced Quasi-Fermi Level Splitting in Molecular Semiconductor Alloys. *Mater. Adv.* **2022**, *3* (13), 5344−5349.
(52) Liu, C.; Yang, Y.; Chen, H.; Xu, J.; Liu, A.; Bati, A. S. R.; Zhu, H.; Grater, L.; Hadke, S. S.; Huang, C.; Sangwan, V. K.; Cai, T.; Shin, D.; Chen, L. X.; Hersam, M. C.; Mirkin, C. A.; Chen, B.; Kanatzidis, M. G.; Sargent, E. H. Bimolecularly Passivated Interface Enables Efficient and Stable Inverted Perovskite Solar Cells. *Science* **2023**, *382* (6672), 810−815.
(53) Yang, X.; Luo, D.; Xiang, Y.; Zhao, L.; Anaya, M.; Shen, Y.; Wu, J.; Yang, W.; Chiang, Y.-H.; Tu, Y.; Su, R.; Hu, Q.; Yu, H.; Shao, G.; Huang, W.; Russell, T. P.; Gong, Q.; Stranks, S. D.; Zhang, W.; Zhu, R. Buried Interfaces in Halide Perovskite Photovoltaics. *Adv. Mater.* **2021**, *33* (7), 2006435.
(54) Leijtens, T.; Bush, K.; Cheacharoen, R.; Beal, R.; Bowring, A.; McGehee, M. D. Towards Enabling Stable Lead Halide Perovskite Solar Cells; Interplay between Structural, Environmental, and Thermal Stability. *J. Mater. Chem. A* **2017**, *5* (23), 11483−11500.
(55) McLeod, J. A.; Liu, L. Prospects for Mitigating Intrinsic Organic Decomposition in Methylammonium Lead Triiodide Perovskite. *J. Phys. Chem. Lett.* **2018**, *9* (9), 2411−2417.
(56) Juarez-Perez, E. J.; Ono, L. K.; Qi, Y. Thermal Degradation of Formamidinium Based Lead Halide Perovskites into Sym-Triazine and Hydrogen Cyanide Observed by Coupled Thermogravimetry-Mass Spectrometry Analysis. *J. Mater. Chem. A* **2019**, *7* (28), 16912−16919.
(57) Su, J.; Liu, Q.; Hu, T.; Zhang, X.; Sun, N.; Jiang, S.; Gu, D.; Qiu, J.; Zhang, H.; Zhou, Z. Synergistic Dual-Anchor Passivation at Buried Interfaces Enabling High-Efficiency and Stable Perovskite Solar Cells. *J. Phys. Chem. Lett.* **2025**, *16* (36), 9381−9390.
(58) Pols, M.; Hilpert, T.; Filot, I. A. W.; van Duin, A. C. T.; Calero, S.; Tao, S. What Happens at Surfaces and Grain Boundaries of Halide Perovskites: Insights from Reactive Molecular Dynamics Simulations of CsPbI3. *ACS Appl. Mater. Interfaces* **2022**, *14* (36), 40841−40850.

https://doi.org/10.1021/acsenergylett.5c03637
ACS Energy Lett. 2026, 11, 3755−3763